File S2

S. 1

S.1.1 Simplified Implementation Based on Discrete Fourier Series Decomposition

To estimate *spatial uncertainty*, we first compute the time series of statistical metrics for the temperature field within the neighborhood region $W(P_0)$. The spatial standard deviation at each time step is used to characterize spatial uncertainty:

$$\bar{\sigma}_{\text{space}}(t) = \text{std}\big(t, W(P_0)\big) \tag{S1}$$

The corresponding mean temperature time series is denoted as:

$$Z(t) = \mu\big(t, W(P_0)\big) \tag{S2}$$

To estimate *temporal uncertainty*, we take the time series $Z(t)$ as the baseline signal. Using two years of background data, we apply a sliding window of 365 days to compute the temporal gradient: $\frac{dZ(t)}{dt}$, which is used to construct the fluctuation series for solving the energy balance equation.

Given the substantial challenges in obtaining precise parameters for anomaly discrimination, we introduce an *energy-cycle equilibrium constraint* to regularize the model structure. Notably, this constraint implies that if a primitive function satisfying the energy balance can be accurately recovered, the dependence on temporal uncertainty can be substantially reduced, thereby simplifying the model without compromising its physical relevance.

Leveraging the intrinsic advantages of trigonometric functions in periodic analysis, we propose an *analytic framework* for the rapid estimation of key parameters. Within this framework, we present an effective approach to recover and interpret periodic variability by decomposing the signal into a *discrete Fourier series (DFS)* structure. This decomposition captures the distinct spectral blocks associated with different temporal scales and allows us to interpret underlying physical drivers—especially external forcing—affecting real surface temperature variations.

The DFS-based structure enables a principled classification of discrete signals according to their spectral features. It distinguishes frequency components that conform to the assumption of annual periodicity (e.g., subannual and annual components) from those that deviate from it (e.g., irregular fluctuations and multi-year cycles), thereby providing more reliable parameter inputs for thermal anomaly identification.

To characterize periodic thermal variations with an annual cycle $T = 365$, we begin with the classical Fourier series expansion of a continuous temperature function $f(t)$:

$$f(t) = a_0 + \sum_{k=1}^{\infty}\left[a_k \cos\left(\frac{2\pi k}{T}t\right) + b_k \sin\left(\frac{2\pi k}{T}t\right)\right] \tag{S3}$$

with the coefficients defined as:

$$\begin{cases} a_0 = \dfrac{1}{T}\displaystyle\int_0^T f(t)\,dt \\ a_k = \dfrac{2}{T}\displaystyle\int_0^T f(t)\cos\left(\frac{2\pi k}{T}t\right)dt \\ b_k = \dfrac{2}{T}\displaystyle\int_0^T f(t)\sin\left(\frac{2\pi k}{T}t\right)dt \end{cases} \tag{S4}$$

For discrete signals, define sampling times as: $t_n = \frac{365n}{N}, \quad n = 0,1,\dots,N-1$, Then the discrete Fourier transform (DFT) and its inverse are:$F_k = \sum_{n=0}^{N-1} f(t_n) \cdot e^{-i\frac{2\pi kn}{N}}$, $f(t_n) = \frac{1}{N}\sum_{k=0}^{N-1} F_k \cdot e^{i\frac{2\pi kn}{N}}$.

For real-valued inputs, this reduces to:

$$f(t_n) \approx a_0 + \sum_{k=1}^{\frac{N}{2}} \left[a_k \cos\left(\frac{2\pi kn}{N}\right) + b_k \sin\left(\frac{2\pi kn}{N}\right)\right] \tag{S5}$$

The signal $f(t)$ can be grouped based on spectral structure as:

$$f(t) = f_{k=1}(t) + f_{k>1}(t) + f_{\text{multi-year}}(t) + f_{\text{other}}(t) \tag{S6}$$

where:

$$\begin{cases} f_{k=1}(t) = a_{k_1}\cos\left(\frac{2\pi k_1}{N}t\right) + b_{k_1}\sin\left(\frac{2\pi k_1}{N}t\right), \quad k_1 = \frac{N}{T} \\ f_{k>1}(t) = \sum\limits_{k=\frac{mN}{T}} \left[a_k \cos\left(\frac{2\pi k}{N}t\right) + b_k \sin\left(\frac{2\pi k}{N}t\right)\right], \quad m \geq 2 \\ f_{\text{multi-year}}(t) = \sum\limits_{k=\frac{N}{mT}} \left[a_k \cos\left(\frac{2\pi k}{N}t\right) + b_k \sin\left(\frac{2\pi k}{N}t\right)\right], \quad m \geq 2 \\ f_{\text{other}}(t) = \sum\limits_{k\in K_{\text{other}}} \left[a_k \cos\left(\frac{2\pi k}{N}t\right) + b_k \sin\left(\frac{2\pi k}{N}t\right)\right] \end{cases} \tag{S7}$$

Under the energy-cycle balance assumption (i.e., $T = 365$), we assume: $f(t) = f_{k=1}(t) + f_{k>1}(t) + C,\ C = f_{\text{multi-year}}(t) + f_{\text{other}}(t) \approx \text{constant}$.

Naturally, some regions may exhibit multi-year energy balance cycles, characterized by slow energy return periodicity, such as those driven by phenomena like the El Niño–Southern Oscillation (ENSO). These long-term periodic variations differ across regions and are not governed by a single, well-defined frequency. As such, their precise cyclical behavior remains unclear and must be subject to preliminary analysis before more detailed investigations can be conducted.

Therefore, the analytically reconstructed background signal $\hat{Z}(t)$ and its derivative $\hat{Z}'(t)$ can be approximated as:

$$\begin{cases} \hat{Z}'(t) = \sum\limits_{k=1}^{m}\sum\limits_{i=1}^{365} A_k \cos(\omega_k t_i + \varphi_k) = 0 \\ \hat{Z}(t) = \sum\limits_{k=1}^{m} \frac{A_k}{\omega_k}\sin(\omega_k t_i + \varphi_k) + B \\ \omega_k = \frac{2\pi k}{365}, \quad k \in \mathbb{N}^+, \quad m \leq \left\lfloor \frac{\text{window}}{3} \right\rfloor \end{cases} \tag{S8}$$

Solving the energy balance problem is thus transformed into a parameter optimization problem—such as least-squares fitting—where the goal is to identify an optimal analytical function. In this framework, ω_k denotes the angular frequency of the k-th harmonic component, while A_k and φ_k represent the corresponding amplitude and phase. The number of terms m is bounded above by the integer floor of one-third the number of available data points. The constant term B is estimated from the mean value of the original periodic function:

$$\bar{B} = \frac{\sum_{j=1}^{366}\sum_{t=j}^{j+364} Z(t)}{366 \cdot 365} \tag{S9}$$

To detect thermal anomalies, we apply a two-year background window with a one-year sliding window (365 days) across a 121-day detection set. The modeled temperature value at time point t_i for the α-th reconstruction is denoted by $g^{\alpha}(t_i)$. The temporal uncertainty at t_i is then given by the standard deviation of model outputs:

$$\sigma_{\text{time}}(t_i) = \sqrt{\sum_{\alpha=1}^{n} \left(g^{\alpha}(t_i) - \bar{g}(t_i)\right)^2} \tag{S10}$$

The model's fitting precision is quantified by the coefficient of determination:

$$R_{\text{squared}} = 1 - \left(\frac{\sigma_{\text{time}}(t_i)}{\sigma_{\text{time,tot}}(t_i)}\right)^2 \tag{S11}$$

where the total temporal variance is defined as:

$$\sigma_{\text{time,tot}}(t_i) = \sqrt{\sum_{i=1}^{n} \left(Z(t_i) - \bar{Z}(t_i)\right)^2} \tag{S12}$$

For the estimation of the spatiotemporal correlation coefficient: due to varying rates of change in surface emissivity across regions, it is critical that the 121-day detection set remains robust against systematic biases. We therefore estimate a relatively stable correlation coefficient based on a two-year dataset and a 365-day sliding window, such as Figure S1.

In this approach, we define two concentric zones—an inner zone U and an outer zone V—representing distinct thermal media with potentially different physical properties. Assuming atmospheric influence is approximately homogeneous within the same zone, the spatiotemporal correlation can be estimated from the heat transfer contrast between the two zones:

$$\rho_i = \frac{\sum_m \left(U_i(t) - \hat{U}_i(t)\right)\left(V_i(t) - \hat{V}_i(t)\right)}{\sqrt{\sum_m \left(U_i(t) - \hat{U}_i(t)\right)^2} \cdot \sqrt{\sum_m \left(V_i(t) - \hat{V}_i(t)\right)^2}} \tag{S13}$$

$$\hat{\rho}_{XY} = \mathbb{E}[\rho_i], \quad i = 1,2,\ldots,121 \tag{S14}$$

S.1.2 Comparative Performance of Model Variants

Any local temperature time series can be decomposed into the following components: (Part A) a component with periodicity of one year, (Part B) components with periodicities of $1/k$ years, where $k \in \mathbb{N}^+$ and $k > 1$, (Part C) components with periodicities of k years, where $k \in \mathbb{N}^+$ and $k > 1$, and an aperiodic or irregular residual component.

Under the assumption of annual energy balance, Part C and the irregular residual are treated as constants, and the model can be simplified to include only Part A and Part B. Nevertheless, interannual variations represented by Part C do not conform to the annual energy balance and exhibit dynamic multi year behavior, which complicates the construction of a unified model. Despite this, comparative analyses involving these components are provided in the supplementary material.

To evaluate the robustness and validity of the model parameters and the resulting computations, three model configurations are tested: Model1 includes only the one year periodic component (Part A); Model2 includes both the one year periodic component (Part A) and the $1/k$ year components (Part B); Model3 incorporates the one year (Part A), $1/k$ year (Part B), and k year (Part C) components.

Model1 includes only the one year periodic component (Part A), which is based on the empirical assumption derived from the annual revolution of the Earth. However, real

world thermal signals may not be strictly limited to this annual periodicity. To address this, we also aim to quantify the contributions of the sub annual (Part B) and multi year (Part C) components across different geographical regions, beyond the dominant one year cycle. Such analysis may help future researchers refine anomaly detection models in a region specific manner.

We compute the relative contributions of Part A, Part B, and Part C in models 2 and 3 within the IPCC climate zones. The spatial distribution of these contributions is shown in Figure S2, providing a comparative view of how multi scale periodic components vary across climatic regions.

To systematically analyze the relative contributions of different components of land surface temperature (LST) and sea surface temperature (SST) across the IPCC AR6 climate zones, we separately examine patterns over land and ocean regions, focusing on the spatial variability of dominant components. In coastal transition zones such as SEA, MED, and CAR, both MED and CAR exhibit a strong dominance of the one year periodic component in both LST and SST. In contrast, SEA displays enhanced contributions from sub annual perturbations. Notably, SEA, MED, and CAR all show relatively high proportions of SST in the combined Part A and Part B components, with the exception of MED where the LST component exhibits a larger contribution from Part C. These patterns may reflect the influence of coastal forcing mechanisms at land ocean interfaces. In inland continental regions of Eurasia, including WSB, ESB, ECA, and TIB, the annual component (Part A) dominates under the one year energy balance assumption. However, the presence of substantial multi year contributions (Part C), despite being smaller than Part A or Part B, suggests that long term variability exists in these inland zones. While such variability cannot be ignored, it remains compatible with the annual energy balance framework (Tiebao Zhang et al., 2021). In South America, regions such as SAM and NES show comparable proportions of Part A and Part B, with minimal contributions from Part C, indicating that the thermal dynamics in these zones are more consistent with the assumptions of model2. Coastal regions such as WNA, NCA, NWS, SWS, WSAF, and EAU exhibit certain common features, yet also present notable differences. These areas are characterized by the coexistence of multiple periodic components, implying the presence of diverse and possibly overlapping driving mechanisms.

In oceanic regions such as SPO, NAO, EAO, SAO, SOO, SIO, EIO, and ARO, Part A accounts for the largest proportion of the temperature signal, indicating that these areas generally conform to the assumptions of model1. However, closer inspection of regions such as SIO, EIO, and ARS reveals a gradual increase in the contribution of Part B as proximity to land increases, suggesting enhanced system complexity near coastal boundaries. This pattern may reflect a climate response mechanism that is more sensitive to rapid perturbations, with certain regions dominated by a single prevailing component. A comparison between oceanic and continental model structures further reveals that sea surface temperature dynamics tend to be simpler, with most marine regions—except for some areas near island chains or continental margins—being well described by model1 and characterized predominantly by the one year periodic component. In contrast, temperature variability over land is more strongly influenced by geographic and spatial heterogeneity, requiring more complex representations such as model2 or model3 to adequately capture the underlying thermal dynamics.

Overall, Figure S2a illustrates how sub annual perturbations (Part B), under the assumption of annual energy balance with a dominant one year periodicity, contribute to deviations from the idealized seasonal cycle. In contrast, Figure S2b highlights the role of multi year perturbations (Part C) when the dominant periodicity deviates from one year. These results provide a structured reference for identifying the spatial distribution of

periodic components and can assist future studies in developing region specific anomaly detection models based on the dominant spectral characteristics of the area of interest.

These findings suggest that both model1 and model2 hold strong potential for anomaly detection in most regions. As the model originates from a physically grounded formulation, it ensures physical interpretability, with each parameter reflecting a defined physical meaning. Prior to further interpretation of the results, a comparative analysis of the model parameters is required to develop a globally consistent framework suitable for large scale comparative studies.

By revisiting the original definitions of thermal anomalies, we identify several critical determinants, including the observed temperature time series, the fitted temperature time series (as an approximation of the true signal), temporal uncertainty, spatial uncertainty, spatiotemporal uncertainty, and the spatiotemporal correlation coefficient. Based on the analytical needs of this study, we consolidate these into four essential parameters. Parameter one (coefficient of determination, R^2): this metric quantifies the agreement between the observed and fitted temperature time series, thereby reflecting the extent to which the model captures the essential periodic characteristics of temperature variability in a given region. Parameter two (spatiotemporal uncertainty): though practical computation follows the workflow shown in Figure 2. This parameter characterizes the heterogeneity of the target region in both space and time. Parameter three (time and space uncertainty ratio): This ratio compares the magnitudes of temporal and spatial uncertainties, thereby indicating the relative dominance of temporal versus spatial variability in the target region. Parameter four (spatiotemporal correlation coefficient): This metric is conceptually related to the thermal penetration index discussed earlier. In the absence of external forcing, a lower spatiotemporal correlation coefficient suggests that the anomaly is more likely to originate from subsurface processes within the region. Conversely, higher values may reflect broader surface interactions. In practice, however, multiple factors must be considered, and this coefficient primarily characterizes the coherence of surface thermal radiation across space and time.

As shown in Figure S3, we can directly compare the four characteristic parameters between land surface temperature (LST) and sea surface temperature (SST) under model1. For the coefficient of determination R^2, SST exhibits consistently higher values than LST across nearly all regions. An exception is the Asian continent, where LST shows relatively stronger responses. For spatiotemporal uncertainty (SU), LST displays significantly larger values than SST in most regions, often exceeding twice the magnitude. This contrast is especially pronounced near the polar regions. Remarkably high SU values are also observed in the Tibetan Plateau and along the western flank of the Andes (TIB and SWS), likely associated with complex terrain and their location along major lithospheric fault zones. Regarding the time and space uncertainty ratio (TSUR), SST is generally dominated by temporal uncertainty, with relatively balanced contributions from temporal and spatial components. In contrast, regions such as NPO, EPO, and REF—spanning parts of the El Niño Southern Oscillation domain—and storm prone zones like RAR, EEU, and ENA exhibit a strong dominance of temporal variability. Such temporal dominance implies faster temperature field changes, which severely limits the feasibility of detecting pre seismic transient heat sources in the absence of highly resolution spatiotemporal data. For the spatiotemporal correlation coefficient (SCC), both LST and SST generally show high values, indicating coherent surface thermal structures. However, SCC for LST is notably lower than that for SST in several regions such as Southeast Asia (SEA), Central Africa (CAF), and Northeast South America (NES), possibly reflecting frequent land ocean thermal exchanges in these regions.

By comparing the four characteristic parameters of LST and SST between model2 and model1, we find that the coefficient of determination R^2 for SST increases to above 90

percent in most regions, while that for LST rises beyond 50 percent across a broad spatial extent. This indicates that model2 captures more sub annual signals, which are highly responsive in the temperature time series, thereby providing further support for our hypothesis of annual cycle energy balance. The time and space uncertainty ratio (TSUR) shows a widespread decreasing trend, primarily due to the reduction in temporal uncertainty associated with the increased R^2, which in turn lowers TSUR values. In contrast, the spatiotemporal uncertainty (SU) exhibits relatively small changes, likely influenced by multiple regional factors. Similarly, the spatiotemporal correlation coefficient (SCC) also remains relatively stable, suggesting both the robustness of the model and the intrinsic spatial heterogeneity of the underlying system. Importantly, when component three is introduced in model3, although R^2 continues to improve, the other three parameters become markedly unstable. This behavior reflects signs of overfitting, where the approximated true signal becomes overly dependent on the two year training dataset. Such results are not necessarily consistent with the actual physical processes. Given that the training data may be affected or contaminated by prior events such as earlier earthquakes or climate anomalies, we emphasize that the model should aim to approximate the true physical variability rather than directly equating the learned sample with the physical reality. Additional discussion on this issue is provided in the Supplementary Materials.

In summary, model2 demonstrates consistently strong performance across the majority of IPCC AR6 regions worldwide, with reliable results observed in more than fifty regional partitions. These findings support the feasibility of adopting model2 as a unified framework for generating globally comparable results at the planetary scale. Moreover, its physically grounded formulation and stability across diverse regions further reinforce its applicability in large scale geophysical investigations.

S.1.3 Model2 Across Evaluation Metrics

To investigate the temporal dynamics and spatial heterogeneity of the systems associated with surface cover layers, we analyze the spatiotemporal distributions of four diagnostic indicators under different model configurations. This approach aims to reveal the structural complexity of thermal processes within target domains by characterizing variations in both time and space. As shown in Figure S4b, the global spatial distribution of the coefficient of determination R^2 under model1 exhibits notably high values over midlatitude oceanic regions in both hemispheres. These include the South Pacific Ocean (SPO), the reference equatorial band (REF), the eastern part of East Asia (EAS), the central South Atlantic Ocean (SAO), the South Indian Ocean (SIO), the central North Atlantic Ocean (NAO), and the northern North Pacific Ocean (NPO). These regions correspond to canonical zones of strong seasonal sea surface temperature cycles, where ocean atmosphere coupling is likely to be tightly regulated by annual solar forcing. The elevated R^2 values indicate that model1, which primarily captures the annual cycle component (component A), effectively characterizes the regular and coherent thermal variations in these areas. This suggests that thermal responses in midlatitude oceans are predominantly governed by periodic external drivers, such as solar radiation and large scale ocean currents, rather than by stochastic or transient processes.

In contrast, under model1, equatorial regions exhibit markedly lower spatiotemporal correlation and reduced coefficients of determination R^2 for both land and ocean surfaces. This pattern is especially pronounced across the equatorial Pacific, including the Equatorial Pacific Ocean (EPO) and Northern Pacific Ocean (NPO) zones, which constitute the core of the El Niño Southern Oscillation (ENSO) system. The weak performance of the annual cycle based model in these areas suggests that thermal variability is likely dominated by sub annual or multi annual components, characteristic of ENSO driven dynamics. Beyond these oceanic centers, the Southeast Asia (SEA) region also demonstrates persistently low R^2 values over both land and ocean domains. This may be attributed to

the complex ocean land coupling prevalent in the Maritime Continent, as well as frequent geodynamic disturbances such as volcanism and tectonic activity. These findings indicate that in equatorial regions, particularly those subject to strong coupled ocean atmosphere interactions and geophysical forcing, model1 alone is insufficient to adequately capture the temporal variability in surface temperature.

We also observe that certain continental highland regions, such as WCA in central Eurasia, TIB in the Tibetan Plateau, and SWS in the western slope of the Andes Mountains, exhibit relatively higher land surface R^2 values under model1 when compared to equatorial zones. However, the coefficients of determination in these areas generally remain below 0.5. This indicates that while annual periodicity contributes to surface temperature variability in these high altitude or inland domains, sub annual, multi annual, or even non periodic processes still play a significant role. These influences may include snow cover dynamics, complex topographic modulation, and synoptic scale atmospheric variability. As such, the simplified annual cycle based model1 is insufficient to fully capture the thermal variability in these structurally and climatically heterogeneous regions.

As shown in Figure S4a and S4c, distinct differences in land and ocean surface R^2 values are observed across regions such as REF and EAS. In these zones, the ocean surface exhibits higher and more steadily increasing coefficients of determination, while the land surface displays greater temporal variability. For instance, the East Asia Summit region shows pronounced fluctuations around 2008 and 2014, which may be linked to regional climate anomalies or land surface feedback mechanisms. In contrast, SEA and SCA display relatively consistent R^2 trajectories across both land and ocean domains, suggesting a more synchronized land ocean coupling likely governed by underlying geographic and thermodynamic coherence, as previously discussed. In the SWS region, a gradual increase in ocean surface R^2 is observed beginning around 2005, followed by a sharp decline after 2009. Meanwhile, the land surface R^2 reaches its peak closer to 2010. Notably, a singular spike in ocean surface R^2 emerges around 2014, potentially reflecting abrupt atmospheric anomalies or oceanic disturbances. Additionally, in the TIB region, a sudden increase in R^2 occurs in 2007, followed by a marked decline in 2017. These dynamics may indicate that the spatiotemporal structure of temperature variability in this high elevation zone is subject to external perturbations in land atmosphere coupling.

In summary, the observed patterns reveal a partial spatial coherence of the annual energy balance associated with component A, particularly over midlatitude oceanic regions. However, in areas with lower R^2 values—such as tropical zones and high elevation mountainous regions—the results underscore the necessity of incorporating sub annual or multi annual components into the anomaly detection framework to more accurately capture region specific thermodynamic variability. These findings further highlight the inherent spatiotemporal complexity of temperature fields in seismically active regions. Of course, when addressing thermal anomaly detection across diverse geographical domains, it remains desirable to employ a unified model that enables large scale comparability. While such an approach may involve trade offs in local accuracy, it enhances the interpretability and generalizability of results, provided that the baseline model maintains sufficient applicability across varying climatic and tectonic settings.

The global spatial distribution of R^2 under model2 reveals a substantial improvement over model1. Most notably, apart from certain island dense terrestrial regions such as Southeast Asia (SEA) and New Zealand (NZ), which still exhibit relatively low R^2 values, nearly all other domains show enhanced model performance. The persistent suppression of seasonal coherence in these regions suggests that annual periodicity may have been obscured by more rapid and intense land ocean atmospheric coupling processes near coastal boundaries. Despite slight reductions in R^2 over high latitude and equatorial ocean zones, nearly all ocean surfaces maintain values above 0.7. This supports the

robustness of model2 in capturing seasonal dynamics regulated by large scale ocean atmosphere interactions. Over most continental interiors, R^2 values exceed 0.5, reflecting the improved sensitivity of the refined model to the spatiotemporal structure of land surface temperatures. In high elevation or geodynamically active regions such as the Tibetan Plateau (TIB) and the northwestern flank of the Andes (SWS), R^2 remains around 0.6, likely reflecting the influence of persistent atmospheric coupling and additional geophysical forcing.

Of course, when comparing model3 with model2, a general increase in the coefficient of determination R^2 is evident. However, regions such as the Tibetan Plateau (TIB) and the northwestern flank of the Andes (SWS) continue to exhibit relatively low values globally, indicating the presence of more complex and irregular land atmosphere interactions that are not easily captured by deterministic seasonal models. Additionally, model3 introduces greater computational complexity, and a detailed discussion of its formulation is provided in the Supplementary Materials. Land surface R^2 values show a marked improvement compared to model1. Importantly, this enhancement does not suppress temporal discontinuities. In fact, interannual shifts around 2015 and 2016—previously obscured under the low baselines of SEA and SCA—become clearly discernible. Similarly, ocean surface R^2 remains consistently higher than that over land, underscoring the structural complexity of underlying terrestrial substrates such as topography and geomorphology. These differences also highlight the distinct characteristics of land atmosphere and ocean atmosphere coupling processes.

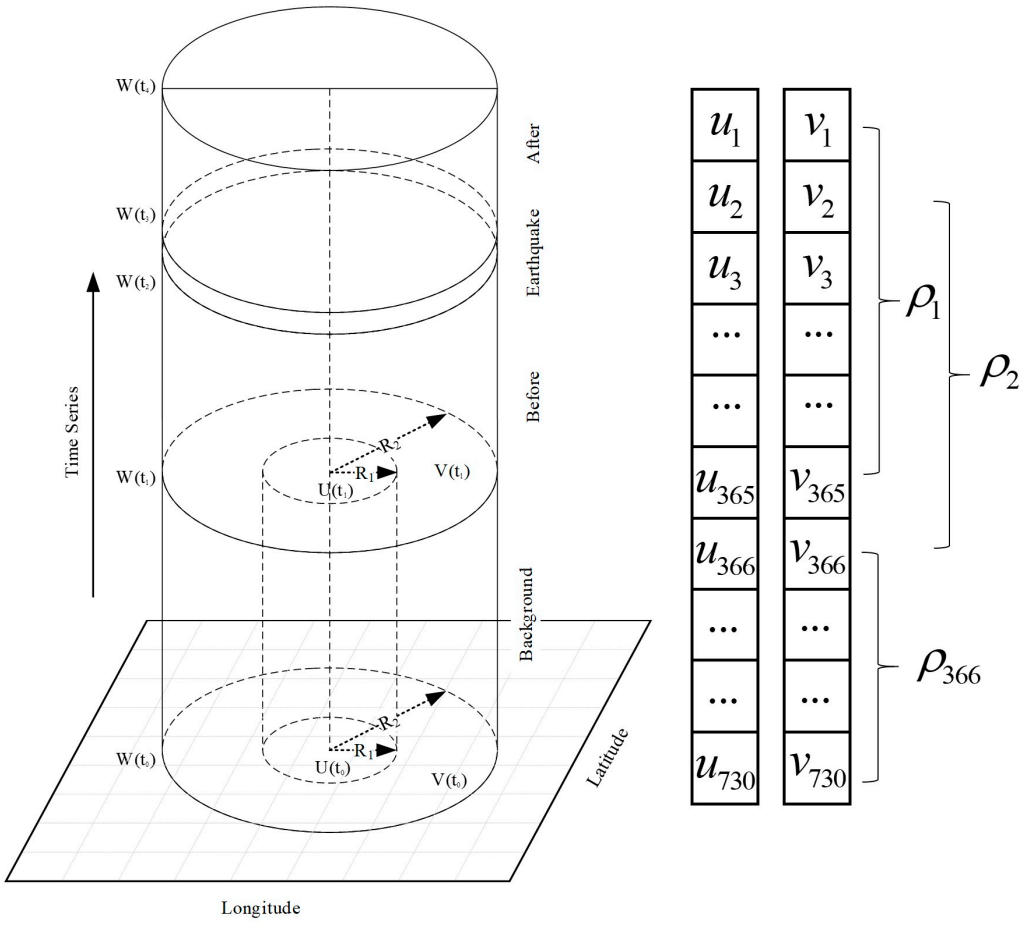


Figure S1 Schematic diagram for estimating spatiotemporal correlation coefficient

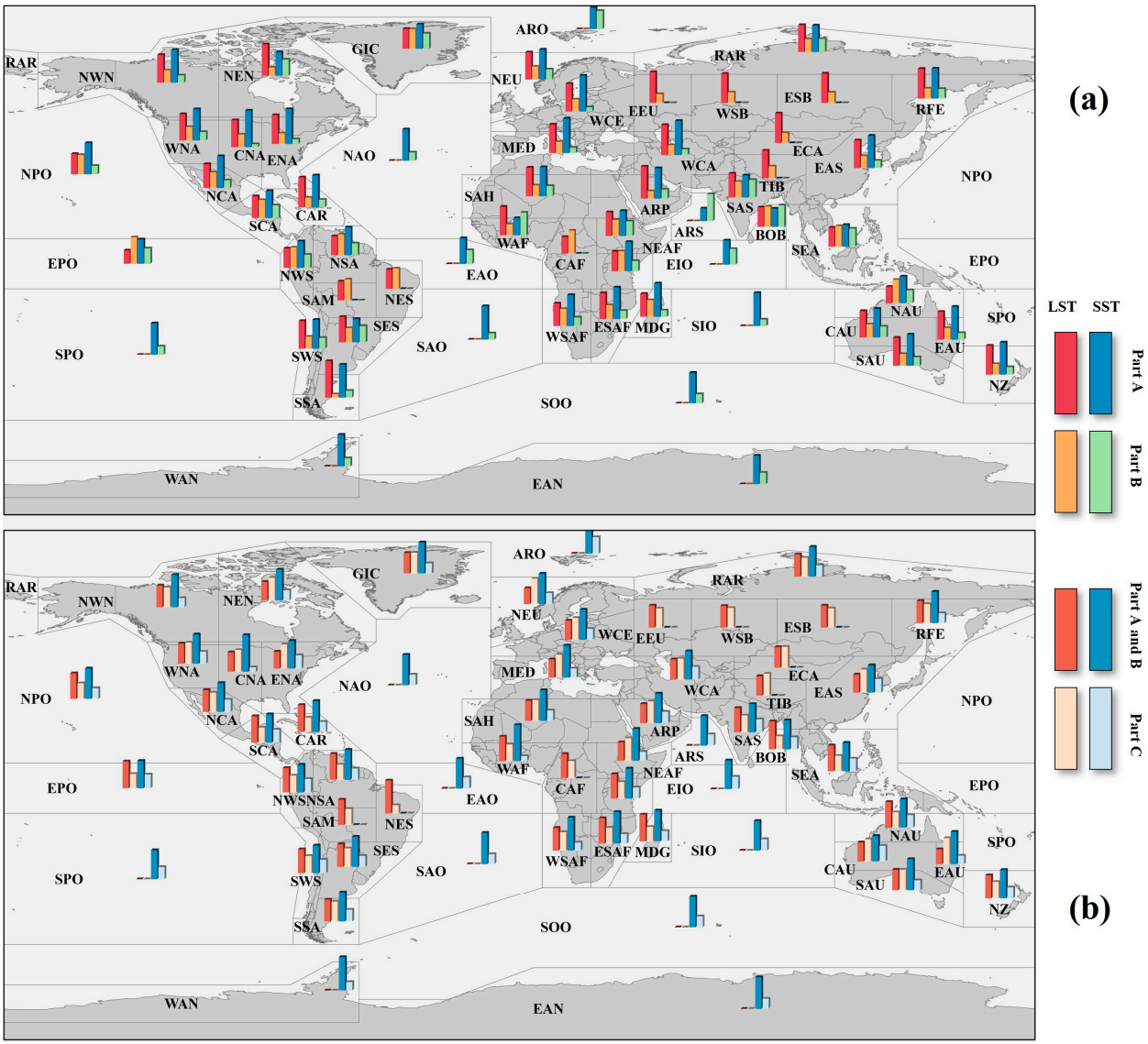


Figure S2 Spatial distributions of periodic component contributions across IPCC AR6 climate zones. (a) Relative proportions of the annual (Part A) and sub annual (Part B) components based on model2. (b) Corresponding proportions of the combined annual and sub annual components (Part A + Part B) and the multi year component (Part C) based on model3. These results are derived from spectral decomposition across 58 distinct climate regions and reflect the varying dominance of periodic signals in different zones.

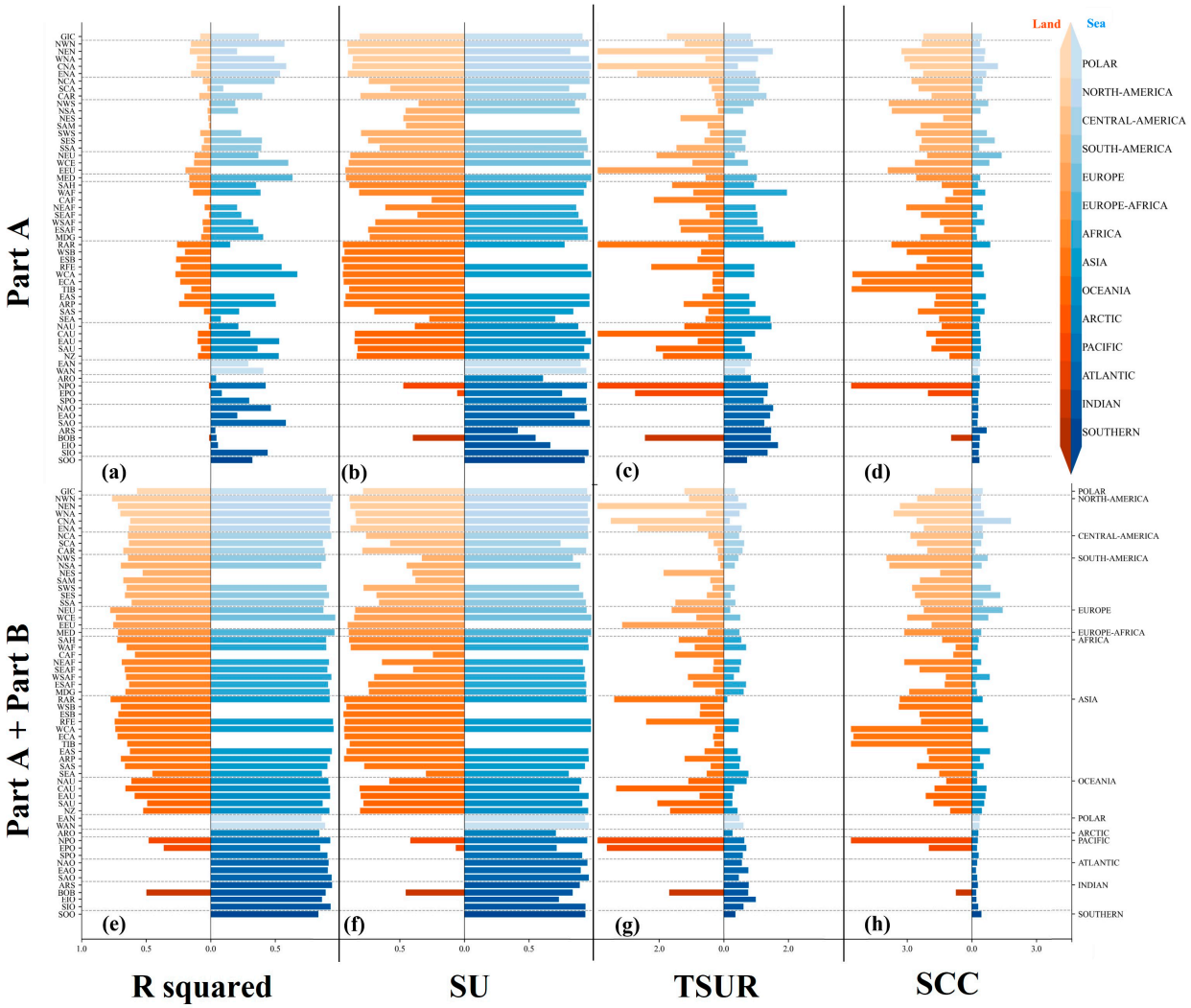


Figure S3 Four characteristic parameters of the annual cycle energy balance model across IPCC regions. Panels a to d represent the parameters for model1, including the coefficient of determination R^2, spatiotemporal uncertainty (SU), time and space uncertainty ratio (TSUR), and the spatiotemporal correlation coefficient (SCC). Panels e to h show the corresponding parameters for model2.

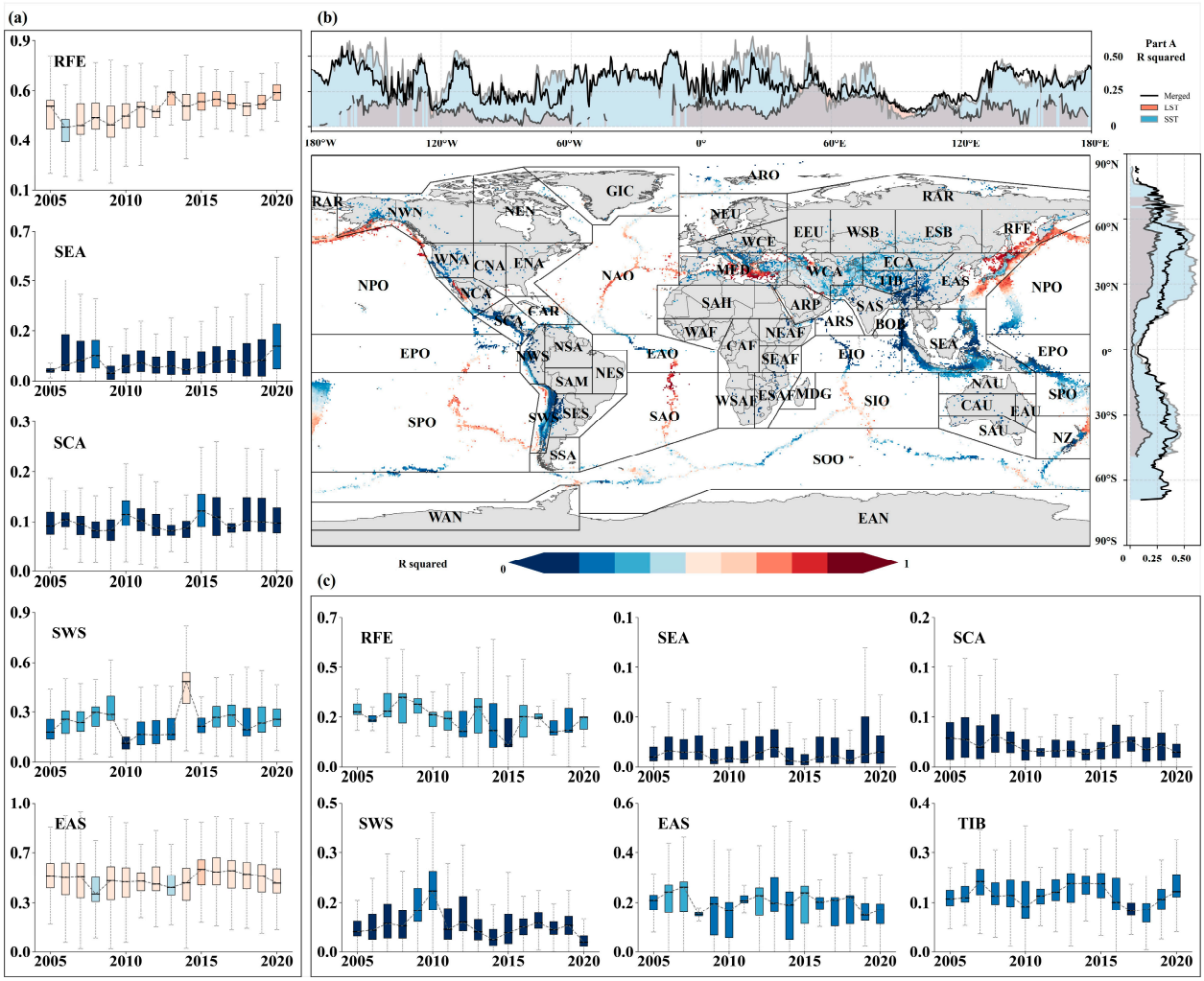


Figure S4 Spatiotemporal distribution of the coefficient of determination R^2 from the independent thermal anomaly detection model based on model1, evaluated across 220,000 global earthquakes. (a) Temporal evolution of R^2 in representative SST regions, including RFE, SEA, SCA, SWS, and EAS. (b) Global spatial distribution of R^2 for the model1 based detection model, with overlays of IPCC AR6 partitions and zonal mean variations along latitude and longitude. (c) Temporal evolution of R^2 in representative LST regions, including RFE, SEA, SCA, SWS, EAS, and TIB.

Reference

1. Tiebao Zhang, Xing Yang, Qian Lu, & Feng Long. (2021). The characteristics of satellite thermal infrared background field in the eastern qinghai-tibet plateau and surrounding areas. Science Technology and Engineering, 21(22), 9217–9223.